Numerical Investigation on Stable Crack Growth in Plane Stress

Cheng Yan and Yiu-Wing Mai

Centre of Advanced Materials Technology, Department of Mechanical & Mechatronic Engineering, The University of Sydney, NSW 2006, Australia

Abstract. Large deformation finite element analysis has been carried out to investigate the stress-strain fields ahead of a growing crack for compact tension (a/W=0.5) and three-point bend (a/W=0.1 and 0.5) specimens under plane stress condition. The crack growth is controlled by the experimental J-integral resistance curves measured by Sun et al. The results indicate that the distributions of opening stress, equivalent stress and equivalent strain ahead of a growing crack are not sensitive to specimen geometry. For both stationary and growing cracks, similar distributions of opening stress and triaxiality can be found along the ligament. During stable crack growth, the crack-tip opening displacement (CTOD) resistance curve and the cohesive fracture energy in the fracture process zone are independent of specimen geometry and may be suitable criteria for characterizing stable crack growth in plane stress.

1. Introduction

Stable crack growth is often observed in elastic-plastic materials prior to catastrophic failure. Ductile tearing resistance of a material is conventionally characterized by the J-integral resistance curve (J_R-curve) which is obtained from bend-type specimens by standard procedure [1]. However, in the plane strain case, the stress triaxiality or constraint in the crack tip region is controlled by the specimen geometry and loading conditions, which gives rise to specimen geometry-dependent J_R-curves [2-6]. Therefore, it is questionable if J_R-curve can be used to characterize the ductile tearing resistance of a material in plane strain. On the other hand, many thin-walled structures and components, e.g., aircraft, pressure vessels and pipelines, are widely used in engineering practice, where plane stress conditions prevail. Some experimental studies indicated that in the plane stress case the initiation toughness is independent of specimen geometry [7-8]. Sun et al [9] showed that for a stationary crack the stress-strain fields are independent of specimen geometry and in good agreement with the HRR solution [10-11]. Sun's experimental work [12] also revealed that the plane stress J_R-curves for different specimens are almost the same. However, little work has been performed regarding the effect of constraint on crack growth under mode I plane stress, notwithstanding its practical importance. Dean [13] and Narasimhan et al [14] have employed finite element methods to study the stress fields ahead of a growing crack under small scale yielding condition. In the present study, large deformation finite element analysis has been carried out to simulate crack tip blunting and subsequent crack growth in compact tension (CT) and three-point bend (SE(B)) geometry with different crack depth.

Mai and Cotterell [7] found that the work performed per unit area in the fracture process zone is a material constant and independent of specimen geometry for sheet

metal of a given thickness. Recently, more attention has been given to microscopic failure processes in the damage or fracture process zone. Barenblatt [15] proposed a cohesive zone model to characterize the non-linear crack behaviour by means of cohesive forces in the fracture process zone. A similar model was proposed by Wnuk [16]. Tvergaard and Hutchinson [17] also incorporated a traction-separation law to analyze stable crack growth under plane strain small scale yielding condition. In the present study, the cohesive fracture energy during stable crack growth in plane stress is also investigated.

2. Material and calculation procedure

The finite element calculations were based on the experimental results of Sun et al [9,12]. The material was a petroleum casting steel and the composition was given in Table 1 [9]. The yield strength of the steel is σ_o=398MPa. The stress-strain relationship is expressed by $\sigma=K\varepsilon^n$, where K=1062 MPa and the hardening exponent n=0.19.

Finite element simulation of stable crack growth was carried out on two specimen geometry, i.e., compact tension (CT) with a/W=0.5 and three-point bend (SE(B)) with a/W=0.1 and 0.5, referred to hereafter as SB1 and SB5, respectively, as shown in Fig.1. The thickness for all specimens was 5.08 mm. Large deformation finite element analysis has been carried out with the finite element code ABAQUS [18]. Four-node isoparametric elements with 2 by 2 Gauss quadrature were used. Only one half of the specimen was modeled because of symmetry. To simulate stable crack growth, small elements with equal width (0.1 mm) are placed in front of the crack tip, as shown in Fig. 2. Rate independent plasticity and associated flow rule were used for the material constitutive model. The yield function for an isotropic hardening materials is

$$f(\boldsymbol{\sigma}) = \bar{\sigma}\ (\varepsilon^{p}) \qquad (1)$$

where $\boldsymbol{\sigma}$ is Cauchy stress, $\bar{\sigma}$ is equivalent stress, and ε^{p} is the equivalent plastic strain. Here f is the Mises yield function,

$$f(\boldsymbol{\sigma}) = \left(\frac{3}{2}\, S_{ij}\, S_{ij}\right)^{\frac{1}{2}} \qquad (2)$$

where $\mathbf{S}_{ij}$ is the deviatoric component of stress. The J-integral was evaluated according to the virtual crack extension technique. Integration contours were taken through the centroids of rings of elements around the crack tip, Fig. 2. After crack growth, the calculated J-integral may depend on the position of integration contours. That is, the J-integral may be path-dependent. In the present study, the far field J-integral is defined as the values which are calculated from the contours far from the crack tip (J_{12} in Fig. 2) and converge to a constant. In this calculation, load was introduced *via* load-line displacement control. Crack growth was achieved by the method of node release incorporated in the ABAQUS code. With crack length prescribed as a function of time, nodal forces of the crack tip elements were released gradually to avoid numerical oscillation and non-convergence. Fine adjustment for node release time is needed to ensure good agreement between calculated far field J with experimental J_R-curves.

3. Results and discussion

3.1 Stress-strain fields

Figs. 3(a)-3(d) show the normalized opening stress, σ_{22}/σ_o, with respect to normalized distance, $X/(J/\sigma_o)$, ahead of the stationary crack ($\Delta a=0$) and the growing crack for these two specimen geometry. As can be seen from these figures there is no difference in the calculated distributions. The opening stress appears to be insensitive to specimen geometry for both stationary and growing cracks. The peak opening stress is about $2.8\sim2.9\sigma_o$ which is greater than the perfect plasticity solution of $2.0\tau_o$ (τ_o=shear yield strength, $2\tau_o=\sigma_o$) obtained by Narasimhan et al [14] and Rice [19]. Also, the peak opening stress remains approximately constant ($2.8\sim2.9\sigma_o$) during stable crack growth. This is different from the stress field under plane strain condition in which the opening stress increases with stable crack growth [20-21]. The variation of equivalent strain, ε_{eq}, for different amount of crack growth is shown in Fig. 4. It is clear that there is a slight increase of ε_{eq} with crack growth. An almost identical ε_{eq} distribution can be found for the two specimen geometry. For plane strain, the work of Shih et al [22] and Wu et al [23] indicated that plastic strain distributions ahead of a stationary crack are dependent on the specimen geometry. At the same load level, the single-edge cracked panel has a greater plastic strain than that of a centre-cracked panel. The distribution of plastic strain ε_{22} in a SB5 specimen at various stages of crack growth is illustrated in Fig. 5. It can be seen that the plastic strain converges quickly to an invariant distribution after sable crack growth. The same ε_{22} distributions have been found for SB1 and CT specimens. These results are similar to the work of Narasimhan et al [14] on small scale yielding in plane stress and Sorensen on anti-plane shear crack growth [24].

The distributions of von Mises equivalent stress for various levels of crack growth in the two specimen geometry are shown in Fig. 6. It is clear that the equivalent stress distributions coincide with each other. This indicates that plastic zones ahead of the

moving cracks are similar and are independent of specimen geometry. In contrast with the plane strain case, the plastic zone is strongly dependent on crack depth and specimen geometry [25-26].

3.2 Constraint for growing crack tip

The experimental work of Sun et al [12] indicated that different specimen geometry have the same far field J-integral resistance curves (J_R-curves) under plane stress conditions. The J-integral calculated from different contours in the CT specimen is shown in Fig.7(a). It is clear that after crack growth, the J-integral is no longer path-independent. The J-integral converges to the same value, i.e., path-independent, only when the integration contour is far from the crack tip (J_{10}, J_{11}, and J_{12}). The calculated far field (J_{12}) J-integral resistance curves for the CT and SE(B) specimens are shown in Fig. 7(b) together with the experimental J_R-curve [12]. Therefore, the far field J-integral resistance curve is not sensitive to specimen geometry. This is in agreement with the experimental results of Sun et al [12]. For the sake of comparison, the crack-tip opening displacement (CTOD) is obtained from the finite element simulation for different amount of crack growth and the CTOD resistance curve is shown in Fig. 8. The definition of CTOD here is the opening displacement of the original crack tip. It is clear that specimen geometry has no effect on the CTOD resistance curve. In the plane strain case, however, many experimental and numerical studies have shown that the crack growth resistance is dependent on specimen geometry due to the different constraint levels [2-6]. Conventionally, the constraint is closely related to the triaxiality, which is presented by the ratio of hydrostatic stress σ_m to the equivalent stress $\overline{\sigma}$. According to the HRR field, the triaxiality in the plane stress case is [10-11]

$$\frac{\sigma_m}{\bar{\sigma}} = \frac{1}{3}\left(\frac{\sigma_{11}+\sigma_{22}}{\bar{\sigma}}\right) = \frac{1}{3}\left[\frac{\tilde{\sigma}_{11}(\theta,n)+\tilde{\sigma}_{22}(\theta,n)}{\tilde{\bar{\sigma}}(\theta,n)}\right] \qquad (3)$$

$\tilde{\sigma}_{11}(\theta,n), \tilde{\sigma}_{22}(\theta,n)$ and $\tilde{\bar{\sigma}}(\theta,n)$ are dimensionless functions, which depend on, θ and *n*. Therefore, for a given material, triaxiality only depends on θ and is independent of specimen geometry. For a stationary crack, identical triaxiality distributions have been observed for different specimen geometry in the finite element calculations of Sun et al [9]. Also, the triaxiality is very close to each other for materials with different hardening exponent (*n*=0.1~0.3). To understand the effect of constraint on stable crack growth, it is necessary to compare the triaxiality distributions ahead of a growing crack for different specimen geometry. However, little work has been done on this topic before. Fig. 9 shows the triaxiality distribution $\sigma_m/\bar{\sigma}$ ahead of a growing crack tip for the CT and SE(B) specimens. Clearly, the triaxiality is independent of specimen geometry for both stationary (Δa=0) and growing cracks. The triaxiality distribution for different amount of crack growth is very similar to that of the stationary crack. Therefore, the specimen geometry independence of crack growth resistance curves (whether the far field J_R-curve or the CTOD resistance curve) can be attributed to the fact that all specimen geometry have a similar triaxiality distribution ahead of both stationary and growing crack tips. Consequently, it can be considered that the resistance curve measured in plane stress case is a proper fracture criterion for characterizing the resistance against crack initiation and growth. The CTOD resistance curve seems to have more potential as compared to the J_R-curve due to the path dependence of the near field J-integral.

3.3 Cohesive fracture energy

As pointed out by Hutchinson [27], non-linear fracture mechanics uses a semi-empirical approach to account for large inelastic effects, and a more basic approach is needed to predict fracture condition by accounting for mechanism of separation at the microscopic level. Recently, considerable attention is drawn to the microscopic fracture process. For elastic-plastic materials, experimental investigations have shown that the fracture process is restricted very near to the crack tip. The cohesive zone model (CZM) was originally proposed by Barenblatt [15], postulating that the effect of atomic or molecular attractions is represented by the traction acting on the separating surfaces in the so-called fracture process zone. The fracture process zone is presented by a micro-scaled strip ahead of the actual crack tip [28-29], as shown in Fig. 10(a). The traction acting on the ligament is a function of separation δ. δ_f is the maximum separation distance when the specific fracture energy is obtained during stable crack growth. Considering the Griffith criterion as identical to the fracture model based on cohesive force, the work of separation per unit area which equals to the cohesive fracture energy is expressed as [17,29]

$$\Gamma_o = \int_0^{\delta_f} T(\delta)\, d\delta \qquad (4)$$

One general formulation of the cohesive law (traction-separation relation) is [28]

$$T = T_o\left(1 - \frac{\delta}{\delta_f}\right)^m \qquad (5)$$

where T_o represents the maximum traction in the cohesive zone and m is an exponent of the cohesive law. m>0 represents a non-uniform distribution of traction and m=0

gives a constant traction in the cohesive zone, as shown in Fig. 10(b). For non-hardening materials, a uniform stress distribution (m=0, $\sigma=\sigma_o$) was assumed in the Dugdale model [30]. It is difficult to obtain the cohesive law by means of experiments. Substituting equation (5) into equation (4) then integrating, Γ_o becomes

$$\Gamma_o = \frac{1}{m+1} T_o \delta_f \qquad (6)$$

Finite element method has been applied to study the cohesive zone [17, 28, 31-32]. The cohesive law (equation 5) was specified on the boundary of a finite element model. The value of m is determined by an iteration process to fit the experimental measurements, e.g., load-deflection curve or crack growth resistance curve. In this study, tractions across the crack tip elements were released as a function of time, which can be adjusted to achieve good agreement between the calculated J_R-curve and the experimental measurement. In Fig. 7(b), good agreement between the calculated J_R-curve and experimental results has been observed. Actually, this cannot be claimed to be the actual cohesive law acting on the crack tip elements. Recently, Tvergaard and Hutchinson [33] have shown that fracture toughness results are not sensitive to the shape of the traction-separation relationship. With the assumption of a constant cohesive law during crack growth, the variation of cohesive fracture energy can be investigated by the present finite element analysis. Based on equation (6), the cohesive fracture energy can be estimated by determining both T_o and δ_f. A similar method was used by Swadener and Liechti [34] to investigate the asymmetric shielding mechanisms in the mixed-mode fracture of a glass/epoxy interface. For simplicity, only the opening stress acting on the ligament is assumed to contribute to

the evolution of the fracture process zone. As can be seen from Fig. 3, the peak opening stress (σ_{22}) ahead of a growing crack has little variation during crack growth. It is quite reasonable to take the peak opening stress ($2.9\sigma_o$) as the maximum traction T_o. According to the cohesive zone model (Fig. 10(a)), the maximum separation δ_f can be obtained from the crack-tip finite element mesh where all traction is lost (σ_{22}=0). Regardless of the absolute value of Γ_o, two extreme cases, i.e., m=0 and 1 are assumed to estimate Γ_o by equation (6). Fig. 11 shows that Γ_o is not sensitive to specimen geometry and is almost a constant during stable crack growth despite some slight variation. This result is similar to the work of Yuan et al [28].

In Fig. 7, the slope of J-integral resistance curves depends on the integration contour. For the contours near to the crack tip, the J-integral, e.g., J_1, is small compared to those calculated from the contours far from the crack tip. This means that in the region near to the crack tip the plastic energy dissipation is relatively small compared to the overall plastic energy dissipation. Also, J_1 increases slightly with crack growth. On the other hand, the J-integral calculated from the contours far from the crack tip increases steadily with crack growth. This shows that the total energy dissipation, i.e., energy of plastic deformation and creation of new crack surface increases during crack growth. When the contour is sufficiently away from the crack tip, the J-integral becomes path-independent (J_{10}, J_{11} and J_{12}).

The length of cohesive zone *l*, as shown in Fig. 10(a), is obtained from the finite element simulation by measuring the point where all traction is lost (σ_{22}=0) and where the maximum traction T_o is first attained ahead of the crack tip. The variation of *l* with crack growth is shown in Fig. 12. The length of cohesive zone is not sensitive to both specimen geometry and crack growth. There is some scatter in the data due to the discontinuous node release in the finite element simulation. The work of Yuan et al

[28] indicated that cohesive zone length is only slightly dependent on the finite element size ahead of crack tip. Also, it can be seen from Fig. 12 that the length of the cohesive zone is very small compared to the ligament of the specimen. In summary, the cohesive fracture energy is nearly constant during crack growth and is independent of specimen geometry. It may be a suitable parameter for characterizing stable crack growth under plane stress condition. This conclusion is in agreement with the finding of Mai and Cotterell [7] for plane stress ductile fracture in thin metal sheets of a given thickness.

4. Conclusions

The effect of constraint on stable crack growth in plane stress is studied. Large deformation plane stress finite element analysis has been carried out to investigate the stress-strain fields ahead of a growing crack for two specimen geometry, i.e., compact tension (a/W=0.5) and three-point bend (a/W=0.1 & 0.5). Also, the variation of cohesive fracture energy with stable crack growth is evaluated. For the elastic-plastic material with power hardening, the distributions of opening stress, equivalent stress and equivalent strain are not sensitive to specimen geometry. Along the ligaments of the different specimens, the opening stress distributions ahead of a growing crack are similar to those of a stationary crack. The J-integral calculated along the contours near to a growing crack tip is path-dependent. But a path-independent J-integral can be obtained by increasing the distance of the integration contour to the crack tip. The crack-tip opening displacement (CTOD) resistance curves are independent of specimen geometry. For both stationary and growing cracks in plane stress, the triaxiality in the crack-tip region is independent of specimen geometry. The cohesive fracture energy in the fracture process zone is nearly constant during crack growth

and is independent of specimen geometry. Based on the present study, the CTOD resistance curve and cohesive fracture energy may be two potential fracture criteria for characterizing stable crack growth under plane stress condition.

Acknowledgments

The authors wish to thank the Australian Research Council (ARC) for the continuing funding of this project. C. Yan acknowledges the OPRS and UPRA provided by the Australian government and the University of Sydney.

References

1. ASTM E1152-87, *Annual Book of ASTM Standards*, Vol. 03.01., (1987) 853-863, Philadelphia.
2. J. Sun, Z. Deng, Z. Li and M. Tu, *Engineering Fracture Mechanics* **36** (1990) 321-326.
3. E. Roos, U. Eisele and H. Silcher, in *Constraint Effect in Fracture, ASTM STP 1171*, (1993) 41-63, Philadelphia.
4. J.R. Bloom, D.R. Lee and W.A. Van Der Sluys, in *Constraint Effect in Fracture, ASTM STP 1171*, (1993) 383-417, Philadelphia.
5. W. Brocks and W. Schmitt, in *Constraint Effects in Fracture: Theory and Applications, ASTM STP 1244*, (1995) 209-231, Philadelphia.
6. J.A. Joyce and R.E. Link, in *Fracture Mechanics: 26th Volume, ASTM STP 1256*, (1995) 142-177, Philadelphia.
7. Y.W. Mai and B. Cotterell, *Engineering Fracture Mechanics* **21**(1985) 123-128.

8. H.T. Deng and T. C. Wang, in *Advances in Fracture Research* (*Proc. ICF7)* V.1 (1989) 323-327.

9. J. Sun, Z. Deng and M. Tu, *Engineering Fracture Mechanics* **37** (1990) 675-680.

10. J. W. Hutchinson, *Journal of Mechanics and Physics of Solids* **16** (1968) 13-31.

11. J. R. Rice, G. F. Rosengren, *Journal of Mechanics and Physics of Solids* **16** (1968) 1-12.

12. J. Sun, *Effect of triaxiality on ductile damage and elastic-plastic fracture*, Ph.D. thesis, Xian Jiaotong University, (1989), Xian, China.

13. R. H. Dean, in *Elastic-Plastic Fracture: Second Symposium, Volume I-Inelastic Crack Analysis, ASTM STP 803*, (1983) 39-51, Philadelphia.

14. R. Narasimhan, A.J. Rosakis and J.F. Hall, *Journal of Applied Mechanics* **54** (1987) 838-853.

15. G.I. Barenblatt, *Advances in Applied Mechanics* **7** (1962) 55-129.

16. M.P. Wnuk, *Journal of Applied Mechanics* **41** (1974) 234-242.

17. V. Tvergaard and J.W. Hutchinson, *Journal of Mechanics and Physics of Solids* **40** (1992) 1377-1397.

18. ABAQUS User's manual, Version 5.4, Hibbitt, Karlsson and Sorensen, Providence, R.I (1996).

19. J.R. Rice, in *Mechanics of Solids*, (1982) 539-562, Oxford.

20. N.P. O'Dowd, C.F. Shih and R.H. Dodds, Jr, in *Constraint Effect in Fracture: Theory and Application, ASTM STP 1244*, (1994) 134-159, Philadelphia.

21. C. Yan, Y.W. Mai and S.X. WU, *International Journal of Fracture* (1998), in press.

22. C.F. Shih and M.D. German, *International Journal of Fracture* **17** (1981) 27-43.

23. S.X. Wu, Y.W. Mai, B. Cotterell and C.V. Le, *Acta Metallurgica* **39** (1991) 2527-2532.

24. E.P Sorensen, *International Journal of Fracture* **14** (1978) 485-500.

25. W. A. Sorem, R. H. Dodds, Jr and S.T. Rolfe, *International Journal of Fracture* **47** (1991) 105-126.

26. A. M. Al-Ani and J.W. Hancock, in *Advances in Fracture Research* (*Proc. ICF7)* V. 6 (1989) 3817-3826.

27. J.W. Hancock, *Journal of Applied Mechanics* **50** (1983) 1042-1051.

28. H. Yuan, G. Lin and A. Cornec, *Journal of Engineering Materials and Technology* **118** (1996) 192-200.

29. J.R. Rice, *Journal of Applied Mechanics* **35** (1968) 379-386.

30. D.S. Dugdale, *Journal of Mechanics and Physics of Solids* **8** (1960) 100-108.

31. P.E. Roelfstra, and F.H. Wittmann, in *Fracture Toughness and Fracture Energy*, Elsevier Applied Science, London (1986) 163.

32. F.H. Wittmann et al., *Mater.Struct.* **21**(1988) 21.

33. V. Tvergaard, and J.W. Hutchinson, *Philosophical Magazine* **70** (1994) 641-656.

34. J.G. Swadener, and K.M. Liechti, *Journal of Applied Mechanics* **65** (1998) 25-29.

Table 1. Chemical composition of petroleum casting steel (%)

C	Si	Mn	P	S	Cr	Mo	Ni
0.36	0.28	1.28	0.015	0.01	0.03	0.01	0.01

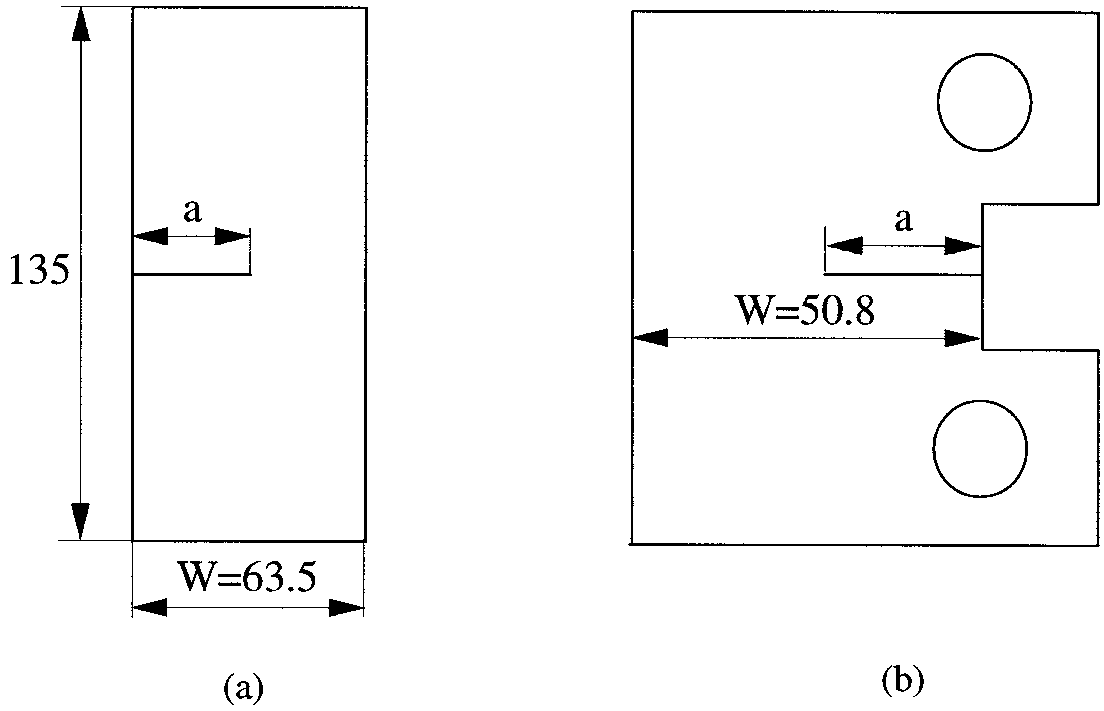

Fig. 1 (a) Three-point bend [SE(B)] specimen (a/W=0.1 and a/W=0.5), and (b) compact tension (CT) specimen (a/W=0.5, all dimensions in mm).

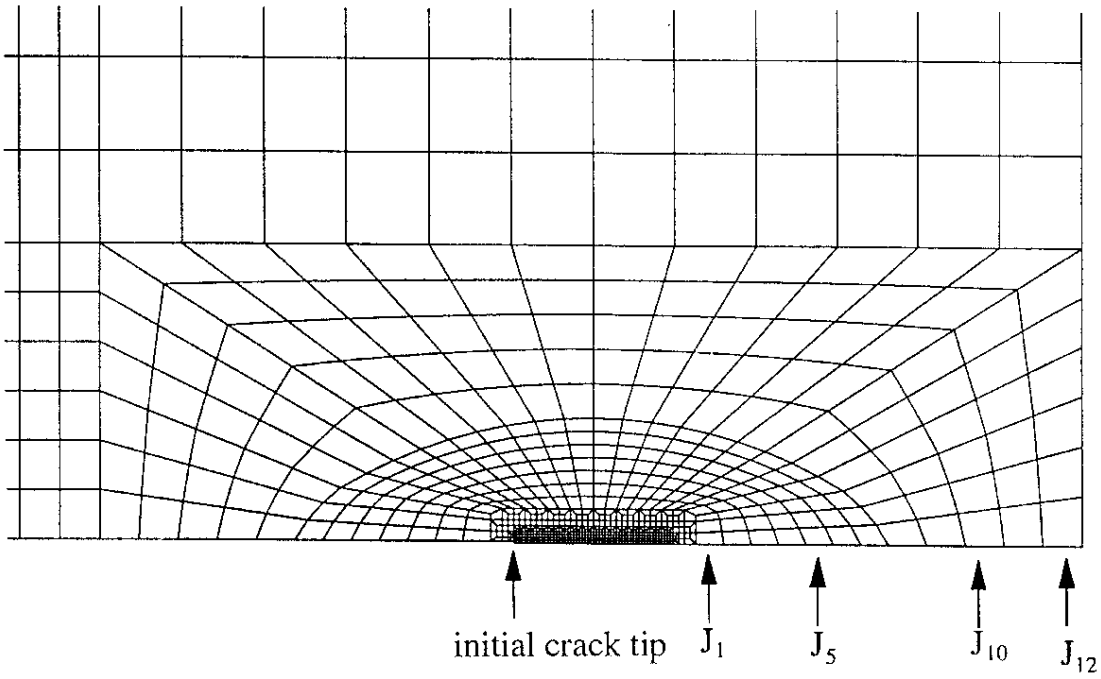

Fig. 2 Finite element mesh at crack tip.

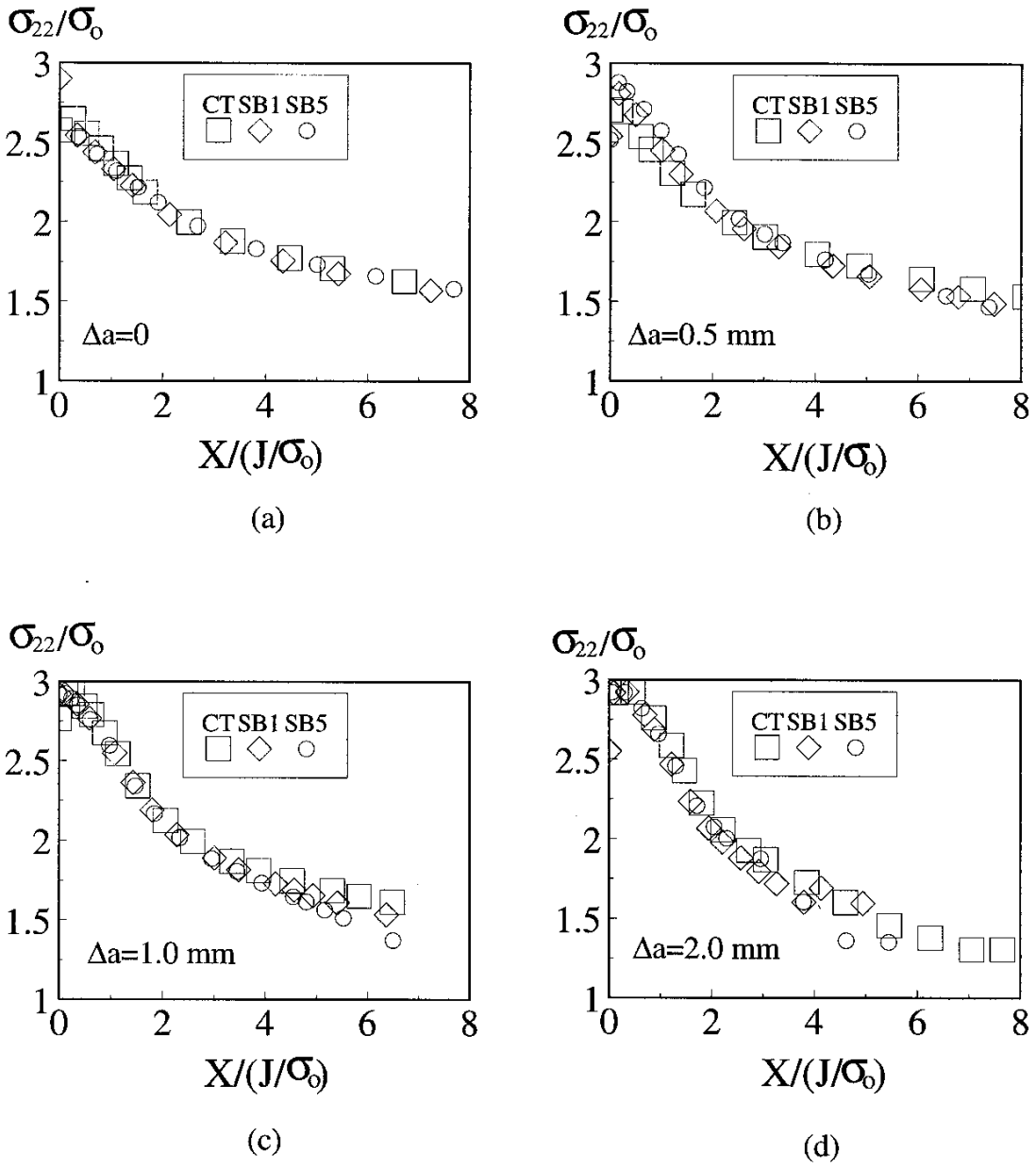

Fig.3 Opening stress ahead of crack in CT and SE(B) specimens: (a) Δa=0, (b) Δa=0.5 mm, (c) Δa=1.0 mm, and (d) Δa=2.0 mm.

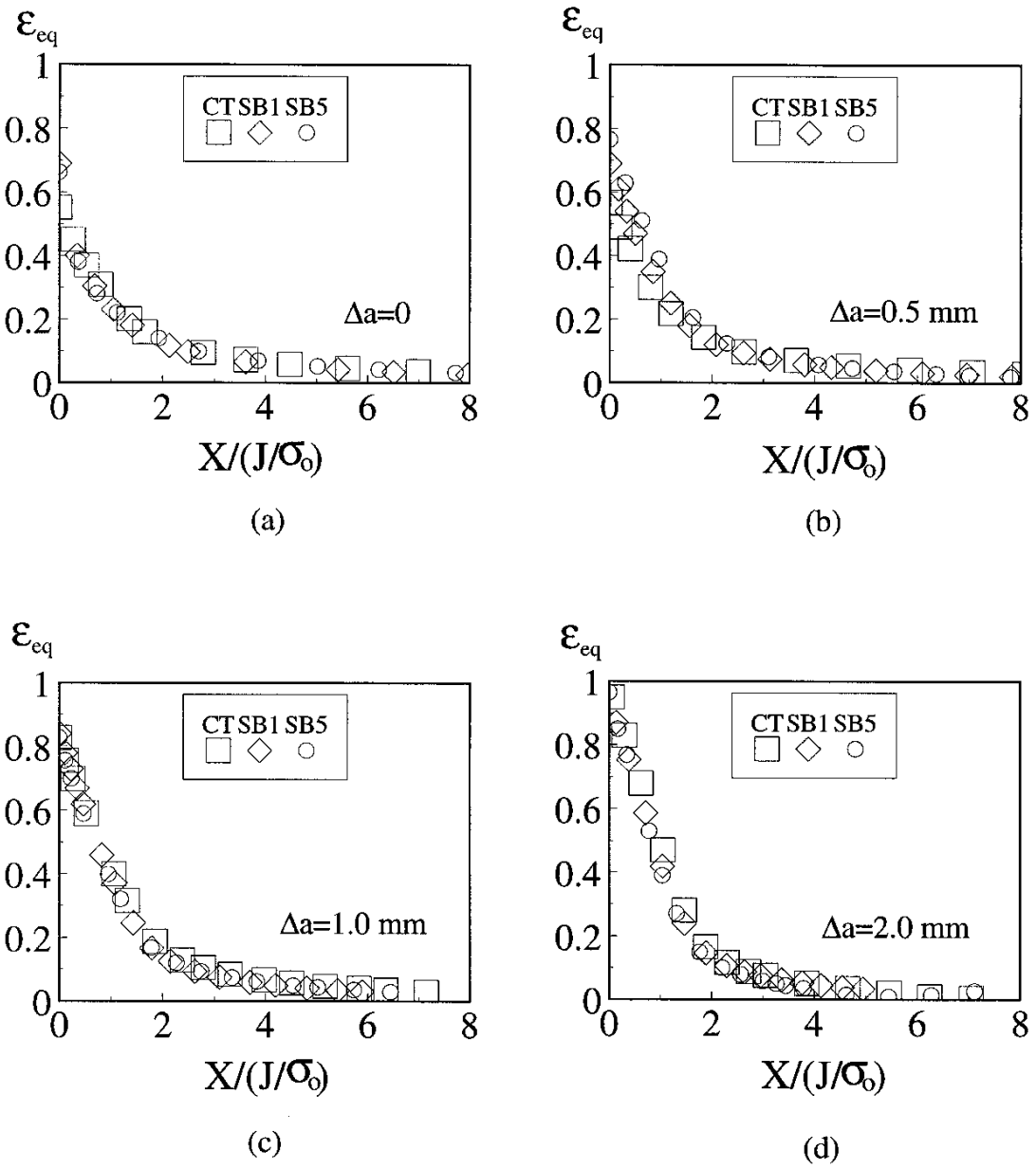

Fig. 4 Equivalent plastic strain ahead of crack in CT and SE(B) specimens: (a) Δa=0, (b) Δa=0.5 mm, (c) Δa=1.0 mm, and (d) Δa=2.0 mm.

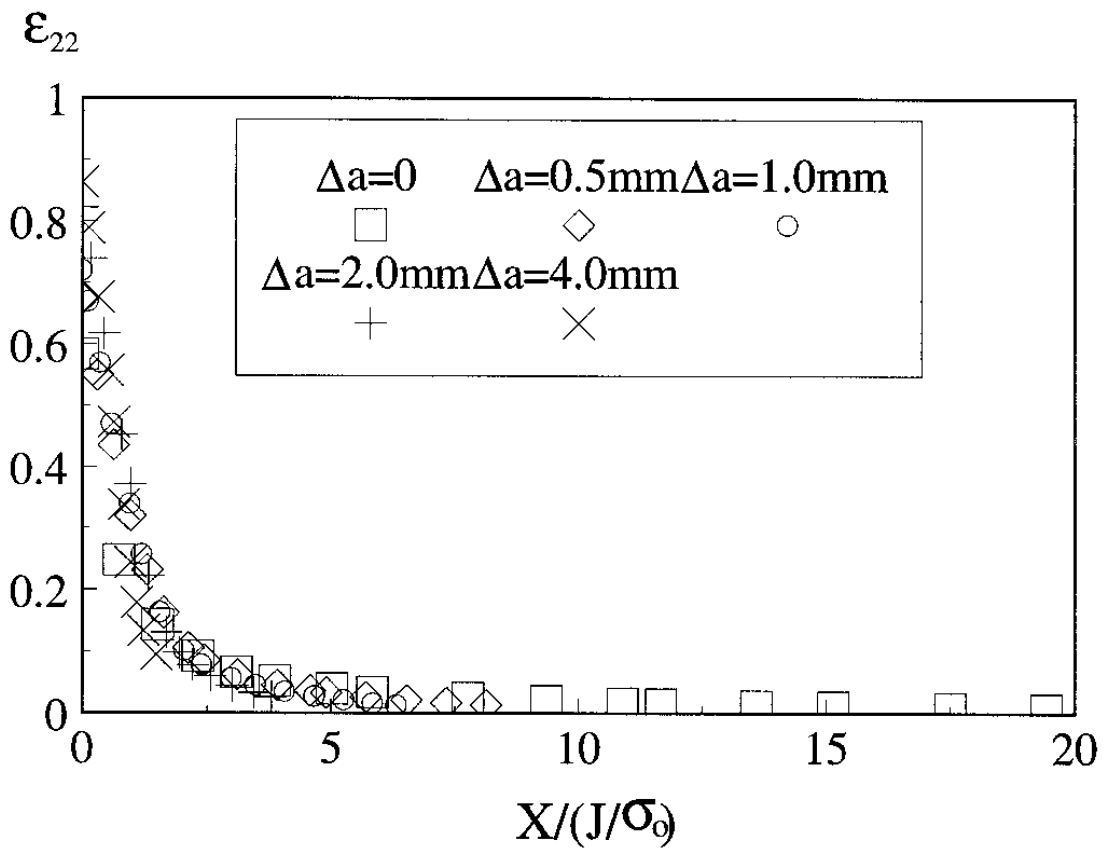

Fig. 5 Variation of plastic strain ε_{22} with crack growth in SB5 specimen.

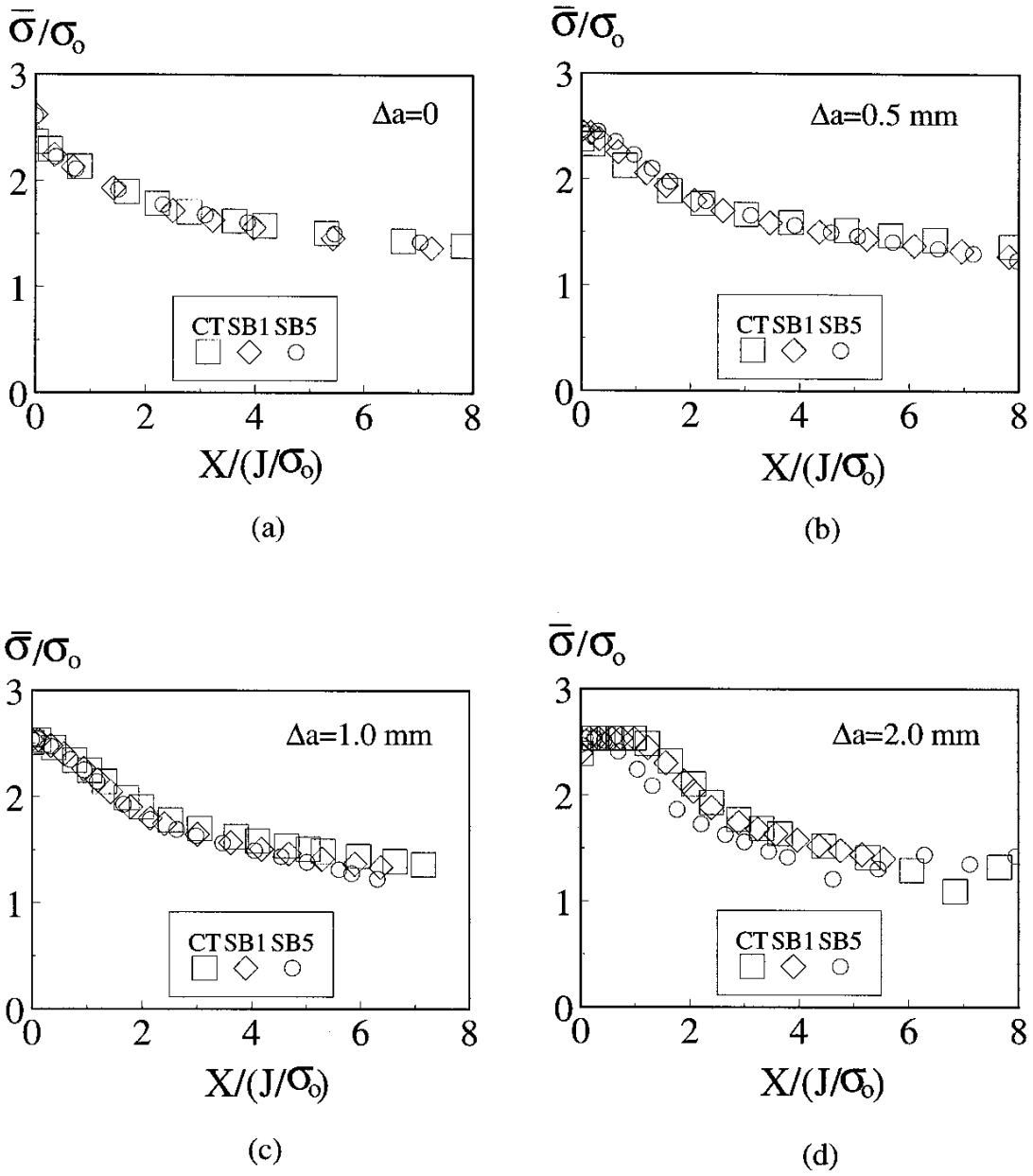

Fig. 6 Equivalent stress ahead of crack in CT and SE(B) specimen: (a) Δa=0, (b) Δa=0.5 mm, (c) Δa=1.0 mm, and (d) Δa=2.0 mm.

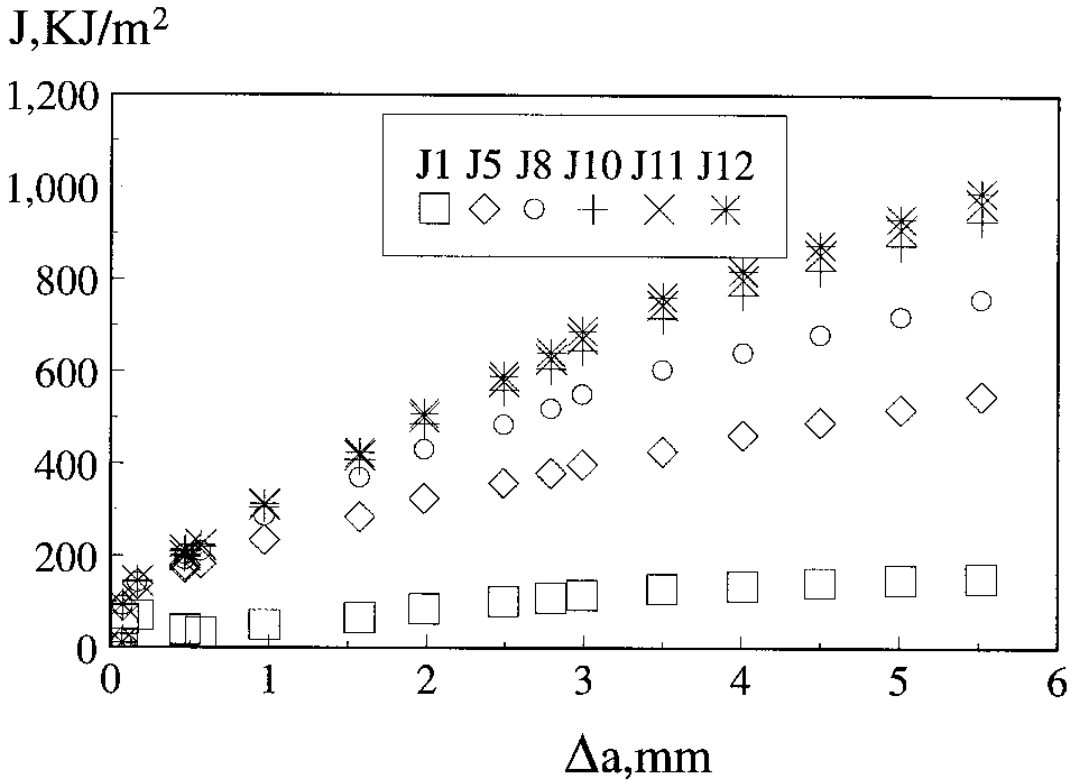
J,KJ/m2
1,200
1,000
800
600
400
200
0
J1 J5 J8 J10 J11 J12
0
1
2
3
4
5
6
Δa,mm

(a)

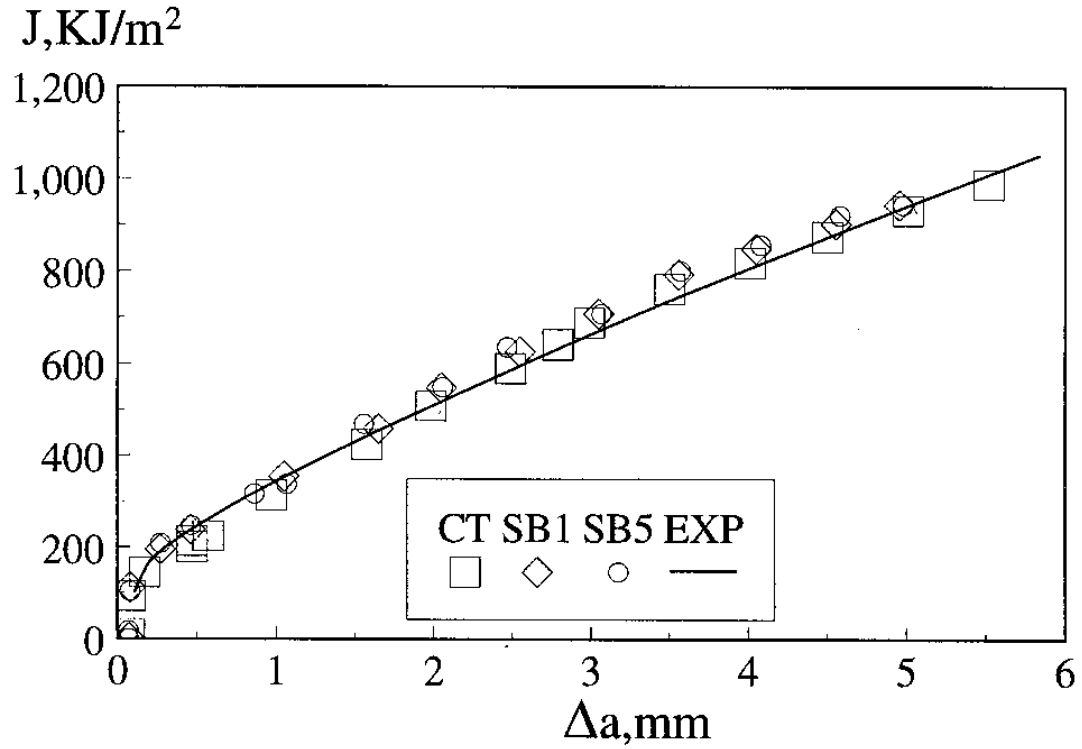
J,KJ/m2
1,200
1,000
800
600
400
200
0
CT SB1 SB5 EXP
0
1
2
3
4
5
6
Δa,mm

(b)

Fig. 7 J_R-curves: (a) from different integration contours in CT specimen, and (b) far field values in CT and SE(B) specimen together with experimental measurement.

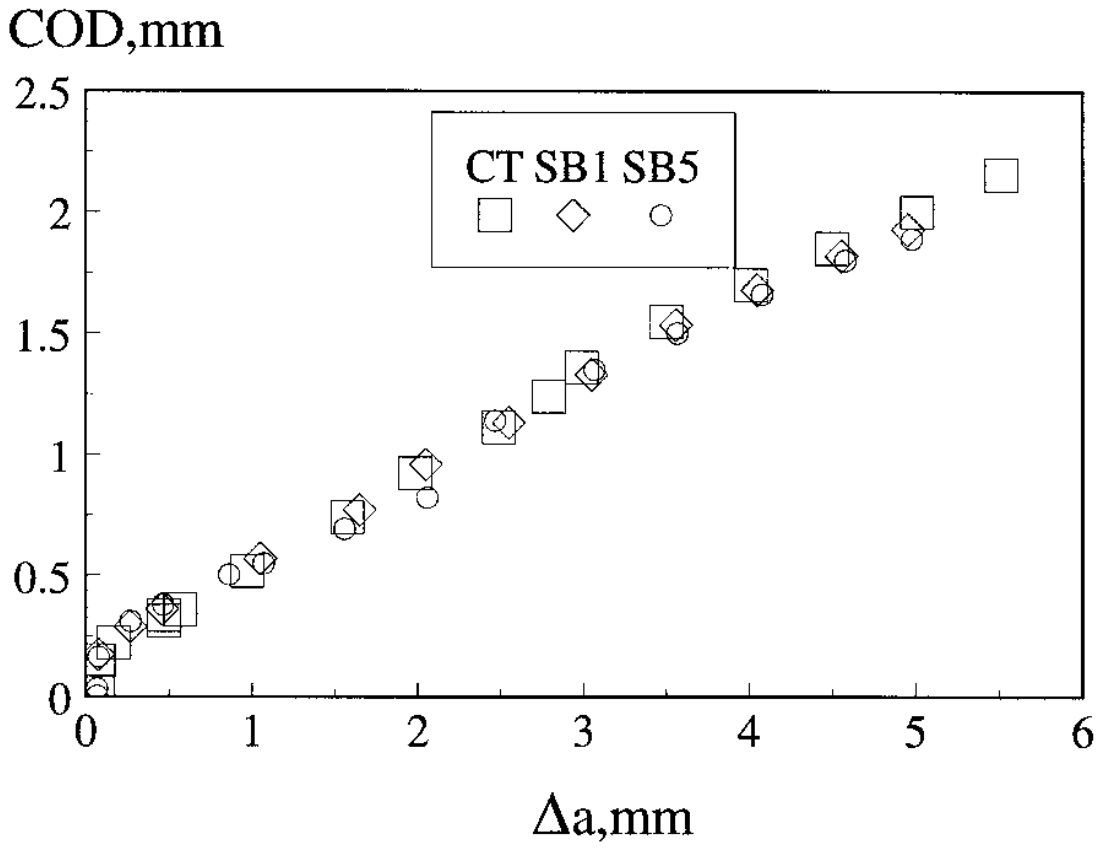

Fig. 8 Calculated crack tip displacement (COD) with crack growth in CT and SE(B) specimens.

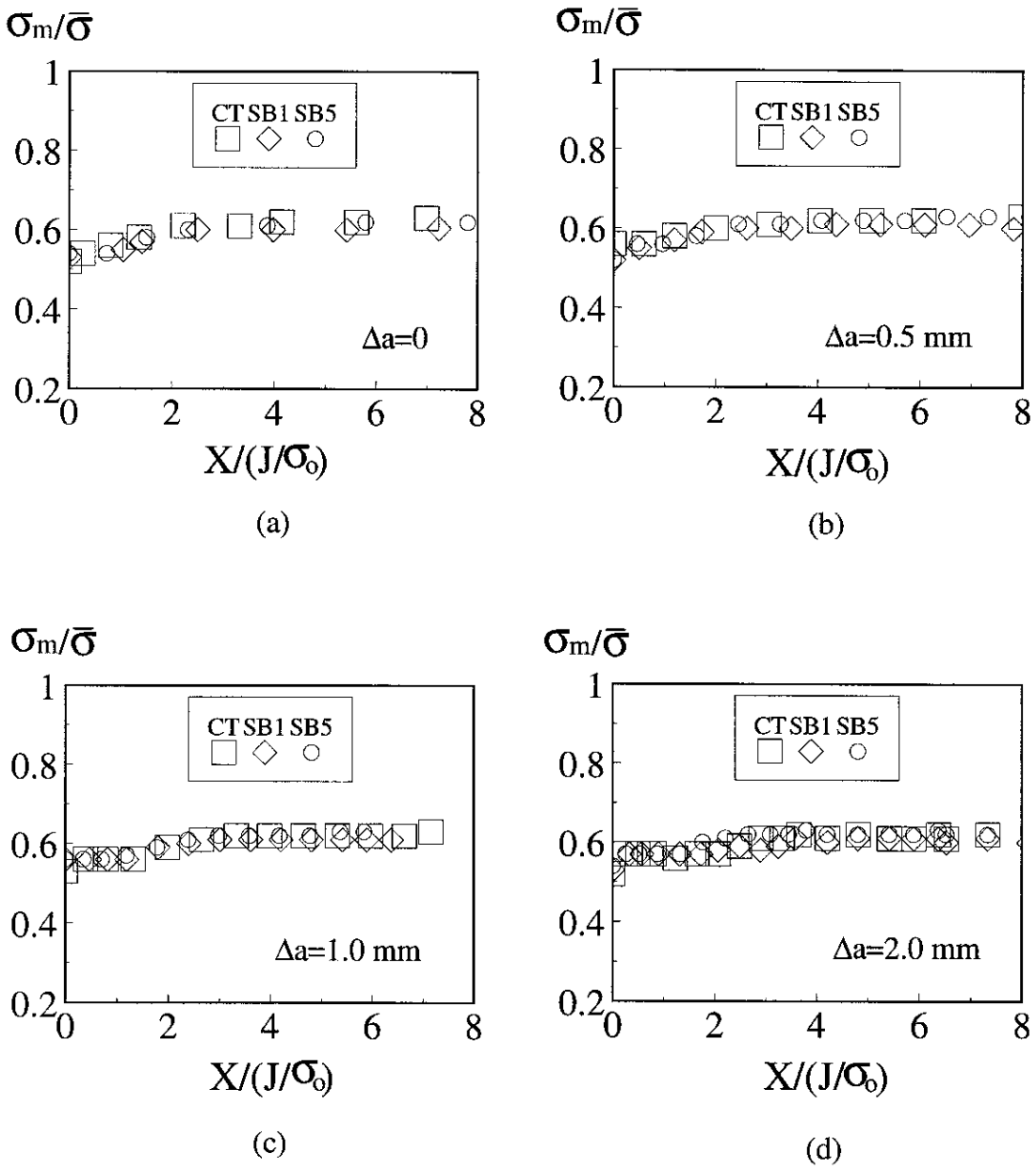

Fig. 9 Triaxiality ahead of crack in CT and SE(B) specimens: (a) Δa=0, (b) Δa=0.5 mm, (c) Δa=1.0 mm and (d) Δa=2.0 mm.

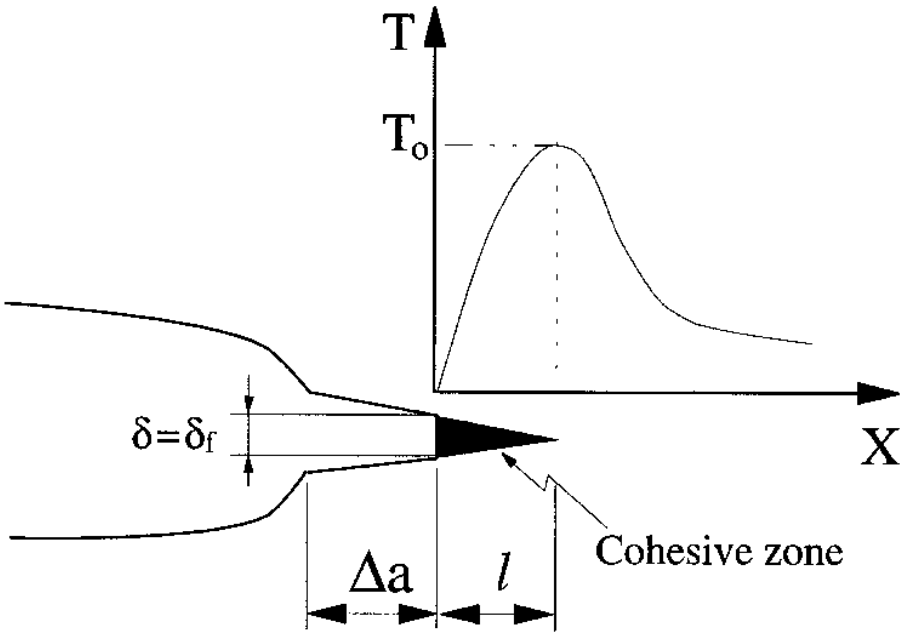

(a)

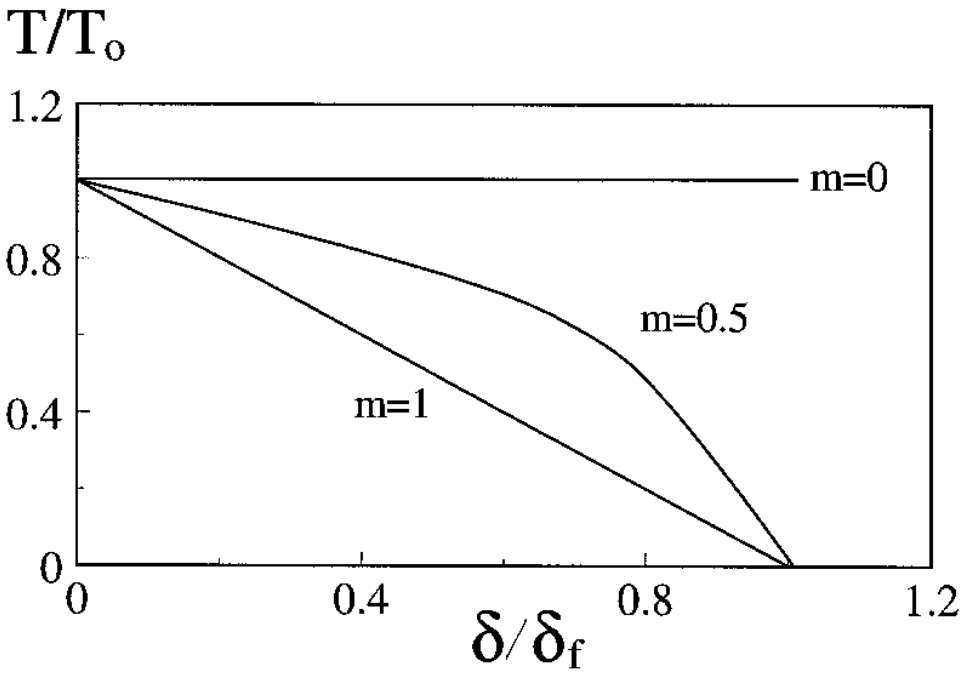

(b)

Fig. 10 (a) Schematic representation of a cohesive zone, and (b) some possible power cohesive laws.

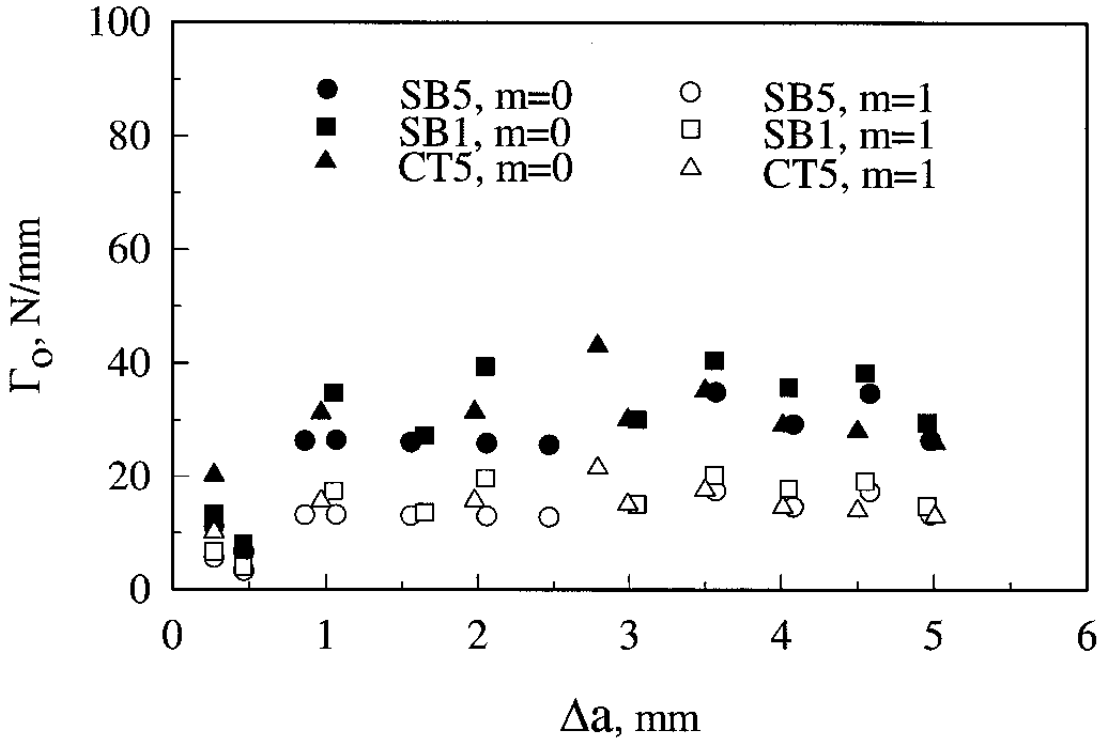

Fig. 11 Variation of specific cohesive energy (Γ_o) with crack growth in CT and SE(B) specimens.

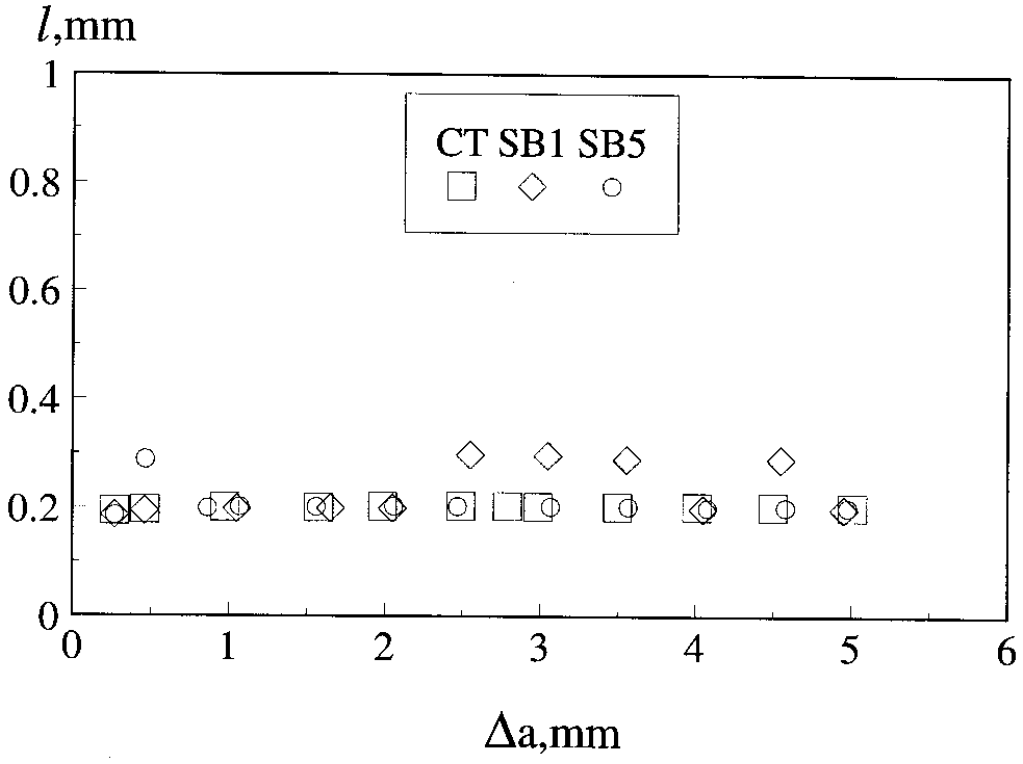

Fig. 12 Variation of length of cohesive zone (l) with crack growth in CT and SE(B) specimens.